Cornered drops and rivulets

J. H. Snoeijer[1,2], N. Le Grand-Piteira[2], L. Limat[2], H.A. Stone[3], and J. Eggers[1]

[1] *School of Mathematics,*

University of Bristol, University Walk,

Bristol BS8 1TW, United Kingdom

[2] *Laboratoire MSC,*

UMR 7057 of CNRS-P7,

10 rue Alice Domon et Léonie Duquet,

75025 Paris Cedex 13, France,

and Laboratoire PMMH,

UMR 7636 of CNRS-ESPCI-P6-P7,

10 rue Vauquelin,

75231 Paris Cedex 05, France

[3] *Division of Engineering and Applied Sciences,*

Harvard University,

Cambridge, MA 02138, USA

We present theoretical and experimental results for a drop of viscous liquid running down an inclined plane at speed U. For $U > U_{cr}$ the rear of the drop forms a corner whose opening half-angle ϕ decreases with U. By matching the interior of the drop to the contact line, we calculate ϕ analytically. We find that above a second critical speed U_{riv} this solution no longer exists and instead a slender rivulet comes out of the tip of the corner. To compute the width of the rivulet, we match to the front of the drop, where it is rounded. Our theoretical results on the opening angle, the rivulet width and the drop velocity are in good agreement with experiment.

I.   INTRODUCTION

The forced motion of contact lines across solid surfaces is fundamental to most coating, painting, and cleaning processes. Its mathematical description represents a challenge, since a moving contact line is not described by hydrodynamics with standard boundary conditions
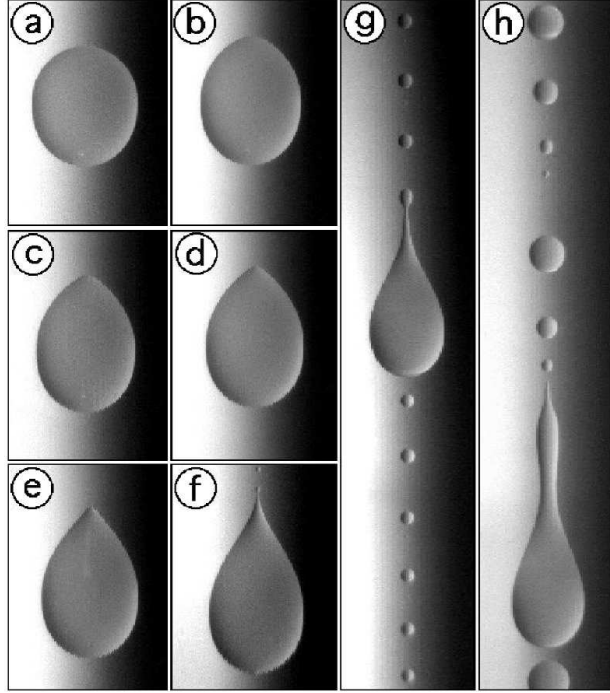
FIG. 1: Drops of silicone oil sliding down planes at increasing inclination angle [5]. As the velocity increases, a corner first forms, which becomes unstable to the ejection of drops at even higher speeds.

[1]. Instead, a microscopic length scale (typically a nanometer [2]) has to be introduced at the contact line [3, 4], which makes the problem multi-scaled.

A particularly important property of contact line dynamics is the asymmetry between advancing and receding contact lines. This feature is illustrated by a viscous drop running down an inclined plane, as investigated experimentally in [5, 6] (cf. Fig. 1), which has an advancing contact line at its front and a receding contact line in its rear. A recent numerical simulation of the same problem has yielded results consistent with experiment [7, 8]. As the inclination angle α of the plane is increased, the drop becomes more and more deformed. However at the front of the drop the contact line remains rounded, while at the rear it undergoes a transformation toward a corner, which indicates the existence of a maximum speed at which the contact line can recede.

A similar asymmetry is observed for plates or fibers plunging into or being withdrawn from a liquid bath. Most often, critical speeds are reported in terms of the dimensionless

capillary number

$$Ca = \frac{\eta U}{\gamma}, \tag{1}$$

where η is the viscosity of the liquid and γ the surface tension of the liquid-gas interface. If the contact line is advancing, the capillary number can be as large as 50 before air entrainment occurs [9], while a receding contact line undergoes a transition at a critical capillary number $Ca_{cr} \approx 10^{-2}$ [10, 11]. Two scenarios are known to be possible: firstly, the contact line may disappear as the fluid is pulled up the solid [11, 12]. As a result, the solid is covered by a macroscopic film known as the Landau-Levich film [13, 14]. The critical speed Ca_{cr} at which the contact line is pulled up has recently been calculated [15] by matching the local contact line motion to the meniscus away from it. A priori, the critical speed of a straight contact line and the speed at which a corner first forms need not be the same, although this is usually assumed. In the present paper, we will not make a distinction between the two speeds.

Secondly, the contact line may incline itself relative to its direction of motion [16], forming the same type of corner that is always observed for a running drop, cf. Fig. 1. As a result, the Landau-Levich transition is effectively *delayed*, and a higher speed can be reached than would be possible for a straight contact line. If the system is sufficiently wide, the contact line can form several corners in an irregular, serrated structure [16]. Clearly, whether the contact line is inclined or not will depend on the boundary conditions, but no predictive theory exists at present.

If the contact line speed is increased even further above a second critical speed Ca_{riv}, a rivulet comes out of the corner of the tip [16]. As is evident from Fig. 1, the same transition is observed for a running drop. The appearance of rivulets is perhaps of even greater technological importance, as it marks the maximum speed at which a steady contact line can be maintained. To avoid confusion, we should mention that similar sequences of transitions are observed eventually for advancing contact lines as well, but at much higher speeds. Presumably, they are associated with the presence of another phase (such as the ambient gas) [17]. Indeed, calculations based on thin-film equations do not provide for any mechanism of a transition in the advancing case [15].

The first theoretical interpretation for the formation of corners goes back to [16], where it is postulated that there exists a maximum speed Ca_{cr} at which a contact line can move. As Ca_{cr} is exceeded, the contact line inclines so as to keep the speed in the direction of its

normal constant:

$$Ca = Ca_{cr}/\sin\phi, \tag{2}$$

where ϕ is the inclination angle, measured from the direction of the motion of the contact line (see Fig. 2). The phenomenological law (2) is in reasonable agreement with experiment [16, 18]. However, the speed-angle law (2) does not define a maximum speed, and thus it appears as if the transition toward a rivulet could only be explained by a local instability near the tip. Below we will show that (2) is only the low-speed limit of a more complete law, which *does not* permit solutions above a critical speed, and thus explains the breakdown of corner solution in a natural way.

In a series of papers, Limat, Stone, and co-workers [19–21] showed that the cornered shape can be understood as a capillary-viscous balance. However, the contact line itself was not included in their description. The flow inside the corner is described by a similarity solution of the thin-film (lubrication) equations. Detailed experiments confirm the structure of the similarity solution [21], but a mechanism that would select ϕ is still missing; it is provided in the present paper.

Once more using a description for thin drops, and a linear relationship between the contact angle and speed, [22] analyzed a running drop by including gravity, but neglecting viscous effects. They found that for arbitrary inclination, the contact line always makes an exact circle. To treat the cornered state, [22] use the condition of constant normal contact line speed to find an opening angle in accordance with (2). Solving the capillary problem in the corner, they propose a condition for the transition to pearling. However, in the rear of the drop, the assumptions made in [22] clearly fail; viscous forces have been shown to be important in the corner region [21], and the macroscopic contact angle no longer follows a linear law as function of speed [23]. By contrast, the front of the drop is described by a circle to a remarkable precision [6].

In the present paper we analyze the running drop as a model problem to understand the formation of corners and rivulets. To that end, we simplify the lubrication equations further by assuming that the drop shape is slender. By matching to the microscopic region around the contact line, we add a condition to the previous similarity theory [20], which selects the opening angle ϕ as function of speed. The resulting speed-angle law deviates from (2) for small angles, and does not allow for solutions above a critical speed. Hence, we predict the maximum speed for cornered contact lines. Above the transition we find novel solutions that
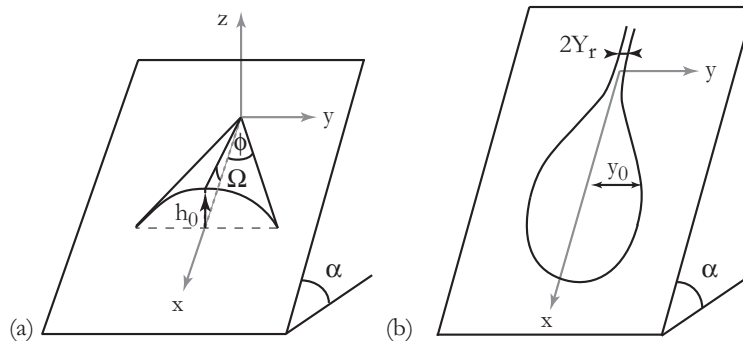
FIG. 2: Sketch of a the drop sliding down an inclined plane. On the left we show the local geometry of the corner, while on the right a rivulet of width $2Y_r$ has formed. The local width of the drop is $y_0(x)$, its thickness at the centerline $h_0(x)$.

correspond to a rivulet of constant width coming out of the tip of the corner, a feature also observed experimentally. To set the width of the rivulet, the solution needs to be matched to the front of the drop, with the influence of gravity included. The resulting drop profiles compare very well to experimental data.

II. HYDRODYNAMIC FORMULATION

A. Lubrication approximation

We consider a drop of viscous liquid whose free surface is characterized by the position $z = h(x, y, t)$. The coordinate axes are defined in Fig. 2. Using the lubrication approximation for thin viscous films, the equation of motion for the free surface becomes [24]

$$3\eta\partial_t h = \nabla \cdot [m(h)\nabla p],\tag{3}$$

where

$$m(h) = h^3 + 3\lambda h^2\tag{4}$$

is called the *mobility*, and λ is the Navier slip length [25, 26], which is about a nanometer for a wetting liquid [27]. In the limit $\lambda = 0$ the classical no-slip condition is recovered, and the contact line cannot move [1]. Many other ways to introduce a microscopic length scale at the contact line have been proposed, for example postulating the existence of a very thin fluid film everywhere on the substrate [8, 28]. However, the choice of cut-off is unlikely to have a significant effect on a macroscopic scale [15, 29].

The flow is driven by both surface tension and gravity, so the effective pressure p is

$$p = -\gamma \triangle h + \rho g(h \cos \alpha - x \sin \alpha), \tag{5}$$

where α is the inclination of the plate. Looking for steady-state solutions for drops sliding at a constant velocity U, i.e. $h(x - Ut, y)$, the equation becomes

$$3Ca\partial_x h = \nabla \cdot [m(h) (\nabla \triangle h + \mathbf{e}_x \sin \alpha - \nabla h \cos \alpha))] \equiv \nabla \cdot \mathbf{j}, \tag{6}$$

where $\mathbf{j}$ represents the flux of liquid with respect to the inclined plate. All lengths have been made dimensionless with the capillary length $\ell_c = \sqrt{\gamma/(\rho g)}$.

Finally, we assume that the interface angle, measured at a microscopic distance from the contact line, equals the equilibrium contact angle θ_e:

$$-\nabla h \cdot \mathbf{n} = \tan \theta_e, \tag{7}$$

where $\mathbf{n}$ is the outward normal to the contact line. For a viscous liquid, (7) is a good approximation if the contact angle hysteresis is small [17]. For the present experiments the hysteresis is typically 5-10° [6].

B. Slender drop equation at the rear

We begin by establishing an asymptotic equation for the drop shape (cf. Fig. 2), valid in the limit that the drop is slender. This approach assumes that the width $y_0(x)$ of the drop is small compared to the streamwise scale x by a factor ϵ, where ϵ is a slenderness parameter. We will see below that to assure a consistent balance, ϵ has to be proportional to the capillary number. If the width of the drop is a constant, corresponding to a long straight rivulet, a parabolic profile

$$h(x, y) = h_0(x) \left[1 - \left(\frac{y}{y_0(x)} \right)^2 \right] \tag{8}$$

is an *exact* solution of (6) with $h_0 = \theta_e y_0/2$, provided that the width is below the capillary length. Otherwise gravity will flatten the profile. Thus for a small drop and to leading order in ϵ, (8) remains valid, but with slowly varying width $y_0(x)$ and centerline height $h_0(x)$. A similar approximation was used recently to describe a thin film of *fixed width*, deposited onto a chemically micropatterned surface [30].

Of course, this simple approximation does not include the logarithmic Cox-Voinov profile expected near a moving contact line [31, 32]. Instead, we use (8) to find an approximate *outer* solution away from the contact line, in which case we can put $\lambda = 0$ in (4) [33]. The Cox-Voinov relation is then used to determine an effective interface angle for the outer problem, which relates $h_0(x)$ to $y_0(x)$. To find another equation for $y_0(x)$ and $h_0(x)$, we integrate (6) over the width of the drop. This step involves the average flux of liquid $\mathbf{j}$ across the rivulet:

$$J(x) = \int_{-y_0}^{y_0} \mathbf{j} \cdot \mathbf{e}_x \, dy, \tag{9}$$

where the total flux $J(x)$ only depends on x. Thus introducing the cross-sectional area

$$A(x) = \int_{-y_0}^{y_0} h \, dy = \frac{4}{3} h_0(x) y_0(x), \tag{10}$$

the y-averaged equation becomes $3Ca\partial_x A = \partial_x J$, which can be integrated once more to obtain

$$3Ca(A - A_0) = J, \tag{11}$$

where A_0 is a constant of integration.

The case $A_0 = 0$ corresponds to closed drops, whereas a positive value of A_0 sets the width of rivulets with straight contact lines parallel to $\mathbf{e}_x$. Namely, liquid gets deposited at zero velocity at the plate, so that inside the rivulet $J = 0$ (apart from a small correction due to gravity, to be given below). In this regime we thus find that $A(x) = A_0$ so that the width of the rivulet becomes

$$y_r = \sqrt{\frac{3A_0}{2\theta_e}}. \tag{12}$$

To evaluate the integral (9), it is useful to once again use the slenderness of the rivulet:

$$Y(\xi) = y_0(\xi/\epsilon), \quad H(\xi) = h_0(\xi/\epsilon), \tag{13}$$

so that the area and the flux become

$$A = \frac{4}{3} HY, \quad J = -\frac{64}{35} \epsilon H^3 Y \left(H/Y^2 \right)' + O(\epsilon^3). \tag{14}$$

For the moment we have neglected gravitational terms, which only become important in the front of the drop.

For $A_0 = 0$, equations (11) and (14) allow for corner solutions, shown schematically in Fig. 2. The characteristic angles ϕ and Ω are related to Y and H by

$$\tan \phi = \frac{dy_0}{dx} = \epsilon Y' \equiv \epsilon \Phi \ , \quad \tan \Omega = \frac{dh_0}{dx} = \epsilon H' \ , \tag{15}$$

and (11) gives

$$\tan^3 \Omega = \frac{35}{16} Ca \tan^2 \phi. \tag{16}$$

This relation between the two opening angles corresponds to the small-angle limit of the corner solutions found in [19, 20], but was shown to be in good agreement over the *whole* range of experimentally accessible angles [21].

To perform the matching to the contact line, missing from earlier descriptions of the corner flow, we now specify the behavior close to the moving contact line. It has been shown that at the contact line the flow becomes two-dimensional, in a direction $\overline{x}$ perpendicular to the contact line [21, 23]. The slope of the profile $\overline{h}(\overline{x})$ close to $\overline{x} = 0$ is thus described by the usual Cox-Voinov relation [31, 32]

$$(\overline{h}_{\overline{x}})^3 = \theta_e^3 - 9\overline{Ca} \ln(\overline{x}/\lambda) \ , \tag{17}$$

where $\overline{Ca}$ indicates the capillary number based on the motion perpendicular to the contact line. We will see below that $\overline{Ca}$ is significantly *below* the critical speed identified in [15], hence the logarithmic profile (17) is still valid. For simplicity, we treat the logarithm in (17) as a constant, $\overline{\ln} = \ln(\overline{x}/\lambda) \approx 10$, and by computing the slope of the profile (8) perpendicular to the flow, we obtain

$$h_0 = \frac{y_0}{2\sqrt{1 + y_0'^2}} \left[\theta_e^3 - 9Ca \frac{y_0'}{\sqrt{1 + y_0'^2}} \overline{\ln} \right]^{1/3} . \tag{18}$$

We are now in a position to identify the slenderness parameter ϵ, and to introduce the scaling

$$\epsilon = \overline{\ln}^{-1/2} \ , \quad \mathcal{C} = \frac{3Ca\overline{\ln}^{1/2}}{\theta_e^3} = \frac{3Ca}{\epsilon \theta_e^3} \ , \tag{19}$$

so to leading order in ϵ, (18) becomes

$$H = \frac{Y\theta_e}{2} \left[1 - 3\mathcal{C}Y' \right]^{1/3} . \tag{20}$$

Thus in the limit of slender drop profiles, $\epsilon \ll 1$, the equation for the drop shape (11) is

$$\frac{35}{6} \mathcal{C} \left[\theta - \left(\frac{Y_r}{Y} \right)^2 \right] = -Y^2 \theta^3 \left(\frac{\theta}{Y} \right)' , \tag{21}$$

where

$$\theta^3 = 1 - 3\mathcal{C}Y' . \tag{22}$$

Equation (21) is the leading-order description for the drop shape in the absence of gravitational effects. Here Y_r is the equilibrium width of a rivulet, which we will compute later, but which is zero in the corner state. In Appendix B, we give an exact solution of (21) and (22) for the case of $Y_r = 0$. Physically, $\theta = \theta_{ap}/\theta_e$ is to be interpreted as a macroscopic or *apparent* contact angle. Namely, extrapolating the profile to the contact line using the present parabolic approximation, one finds θ_{ap}.

III.   THE CORNER

A.   Asymptotic solution at the rear

To find corner solutions of the slender drop equations (21) and (22), we put $A_0 = Y_r = 0$, and assume a constant opening angle Φ, cf. (15). This gives the central result of this paper,

$$\mathcal{C} = \frac{6\Phi}{35 + 18\Phi^2} , \tag{23}$$

shown as the solid line in Fig. 3. The most remarkable feature of (23) is that it possesses a maximum, and thus no corner solutions exist above a maximum speed $\mathcal{C}_{riv}$:

$$\mathcal{C}_{riv} = \sqrt{\frac{1}{70}} \approx 0.12, \quad \Phi_{riv} = \sqrt{\frac{35}{18}} \approx 1.4 . \tag{24}$$

The maximum emerges due to the scaling $\mathcal{C} \propto \Phi$ for small opening angles, a property not foreseen by the earlier prediction of Eq. (2). This scaling can readily be inferred from (16) for small opening angles: in this limit $\Omega/\phi \simeq \theta_e/2$ so that $Ca \propto \phi$. Let us note that this structure of $Ca(\phi)$, exhibiting a maximum speed, was already anticipated in [34]. Above $\mathcal{C}_{riv}$ one has to look for a new type of solutions. We will see below that these correspond to rivulet solutions, thus explaining the transition to liquid deposition beyond a critical drop velocity.
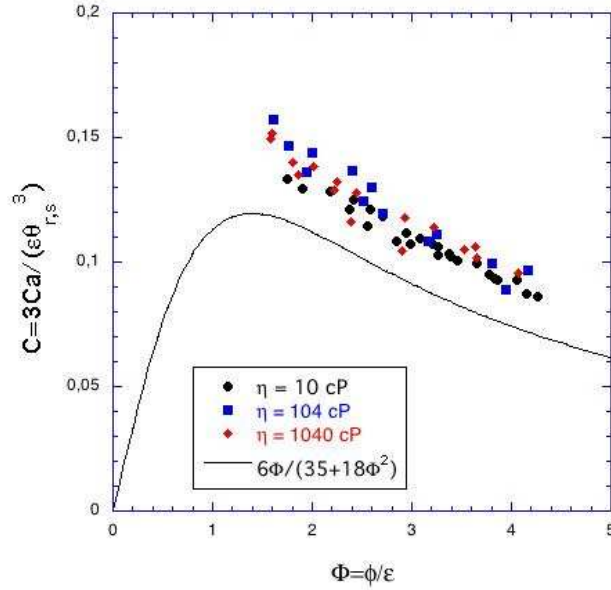
FIG. 3: The normalized speed $\mathcal{C}$ of the drop as function of the normalized opening angle Φ. Symbols represent rescaled experimental data for three different viscosities (see Table I). The data were rescaled using the receding static contact angle θ_r.

Below the critical speed (24), there are two different solution branches of (23), but only the one to the *right* of the maximum is stable. Namely, imagine a perturbation which decreases the angle ϕ, corresponding to a contact line speed, relative to the substrate, which is greater. Relative to the rest of the drop, the perturbed tip position falls behind. But since it moves at a greater speed, the tip catches up and ϕ is restored to its original value. A corresponding argument can of course be made for a slight increase in ϕ. This demonstrates that the right branch of (23) is stable, while for the left branch the signs are reversed, making it unstable.

An experimental measurement of a corner angle ϕ is illustrated in Fig. 4. Away from the tip, the contact line will bend away from a straight line, therefore we attempt to measure the angle as close as possible to the tip. Our theoretical description contains the parameters ϵ and θ_e, which are properties of the contact line. Following [6], they were determined by fitting the Cox-Voinov law (17) to the local slope profile $\bar{h}_{\bar{x}}$ normal to the receding contact line. This leads to values of $1/\epsilon^2$ between 9 and 14 for our three series of measurements,
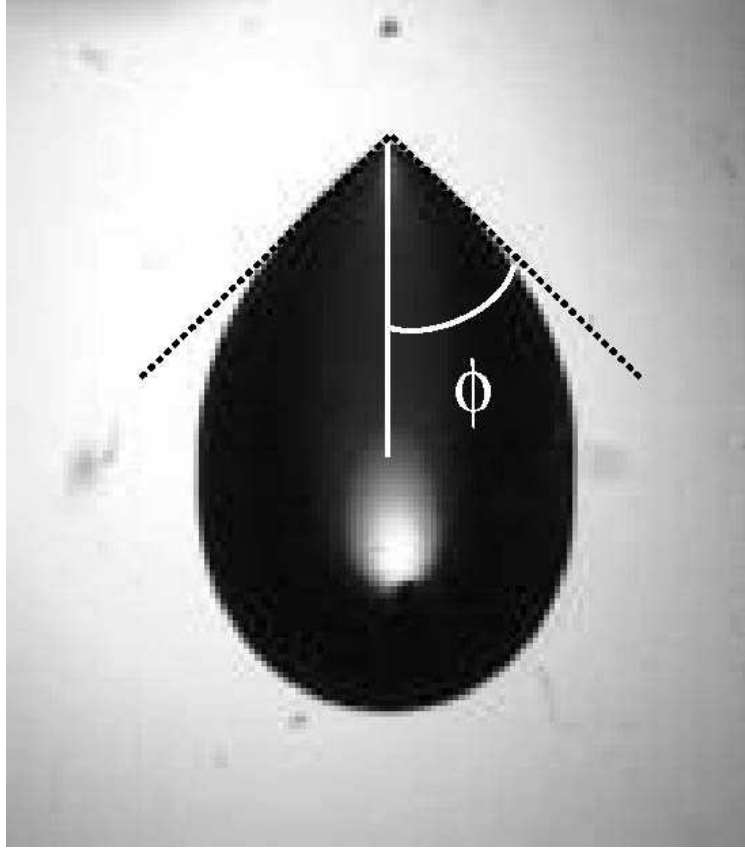
FIG. 4: The angle ϕ is determined by fitting a corner as close as possible to the tip of the drop. The corresponding experimental data are reported in Fig. 3.

using silicone oils with a wide range of viscosities (Table I). Since there is a slight hysteresis [6], the equilibrium angle θ_e has been replaced by the receding contact angle θ_r.

Using the experimentally determined values of θ_e and ϵ, in Fig. 3 we have superimposed the experimental data on the theoretical curve without any adjustable parameters. The data for the three different silicone oils collapse very well when rescaled according to our theory. The minimum angle up to which corners are observed also agrees nicely with theory, while the observed speeds are somewhat larger than predicted. However, one has to keep in mind that the small parameter in our theory is only about 0.3 thus it is not surprising that higher order terms are still significant. In addition, the rescaling of the speed depends very sensitively on the value of θ_r, which can easily contain an error of 5°.

The angle-speed law (23) can be seen as a refinement of the phenomenological equation (2) for small angles, as we will now show. To this end we demonstrate that (23) and (2) are compatible in an overlap region, by taking the large-angle limit $\mathcal{C} = 1/(3\Phi)$ of (23), and

viscosity (cP)	θ_r (°)	ϵ	Ca_{riv} ($\times 10^{-3}$)
10.0	45.5	0.264	5.89
104	42.7	0.331	7.60
1040	46.8	0.344	8.83

TABLE I: Experimental measurements performed on drops of silicon oil sliding on a glass plate coated with fluoropolymers (FC-725 by 3M); for details see [6]. The table displays the receding equilibrium contact angle θ_r and ϵ obtained from fitting the apparent contact angle with Eq. (17) for three different viscosities.

comparing it to the small-angle limit $Ca = Ca_{cr}/\phi$ of (2). Thus if we identify

$$Ca_{cr} = \theta_e^3/(9\overline{\ln}) \; , \tag{25}$$

the two limits become the same. Moreover, (25) is precisely the speed at which the apparent contact angle (22), $\theta^3 = 1 - 3\mathcal{C}\Phi$, goes to zero. This coincides with the condition for the maximum capillary number Ca_{cr} at which a *straight* contact line can recede [15]. However, the present theory is only applicable for small angles, and is therefore not suited to study the transition of a rounded drop toward a corner for which ϕ is close to 90°.

B. Equation for the entire drop

To describe corrections to the linear profile near the tip, and to find the drop speed, we need to describe the shape of the entire drop. In particular, to extend our theory to the front of the drop we have to include gravity in the problem. The front of the drop has a nearly circular profile, as seen experimentally in Fig. 5, which can be understood from a surface tension-gravity balance [22]. The contribution of gravity to the total flux (9) is

$$\int_{-y_0}^{y_0} h^3 \sin \alpha \, dy = \frac{4}{35} \sin \alpha Y^4 \theta^3 \theta_e^3 \; ; \tag{26}$$

the $\cos\alpha$ term has been ignored, since we assume $|\nabla h| \ll 1$. Evidently, the slenderness assumption for $y_0(x)$ breaks down near the front of the drop, where the profile becomes vertical. Indeed, the expression for θ, (22) becomes meaningless in this limit. This can be corrected by returning to the original expression (18), which contains all the geometrical factors. Thus we replace the expression for the apparent angle θ by

$$\tilde{\theta} = \frac{1}{\sqrt{1 + (\epsilon Y')^2}} \left(1 - \frac{3\mathcal{C}Y'}{\sqrt{1 + (\epsilon Y')^2}} \right)^{1/3} , \tag{27}$$

which reduces to θ for $\epsilon \to 0$.

In addition, in the slender drop description the capillary pressure $\Delta h = \partial_{xx} h + \partial_{yy} h$ is replaced by $\partial_{yy} h$. A convenient feature of the pressure-gravity balance found in [22] is that in fact $\partial_{xx} h = 3 \partial_{yy} h$ throughout. Thus by multiplying the capillary term by 4 or, equivalently, dividing gravity by 4, the circular solution is reproduced exactly and (21) becomes (we still are taking $Y_r = 0$):

$$\frac{35}{6} \mathcal{C}\tilde{\theta} = -Y^2 \tilde{\theta}^3 \left(\frac{\tilde{\theta}}{Y} \right)' + \frac{\sin\alpha}{4\epsilon\,\theta_e} Y^2 \tilde{\theta}^3 . \tag{28}$$

This equation has the right behavior both in the back and in the front of the drop. Namely, for small ϵ the corner solution is reproduced, but with a higher-order correction with respect to (23):

$$\mathcal{C} = \frac{6\Phi/B^3}{35 + 18\Phi^2/B^4} , \qquad \text{with} \qquad B = \sqrt{1 + (\epsilon\Phi)^2} . \tag{29}$$

This correction induces a small shift of the critical capillary number, $\mathcal{C}_{riv} \simeq \sqrt{1/70}(1 - 35\epsilon^2/36)$. In the the front of the drop, where the left hand side is small, the circle is indeed found as an exact solution when linearizing (27) with respect to $\mathcal{C}$. Finally, the prefactor of the gravity term can be absorbed into a choice of length scale. If we measure all lengths in units of

$$L = 2\ell_c \sqrt{\theta_e / \sin\alpha}, \tag{30}$$

(28) becomes

$$\frac{35}{6} \mathcal{C}\tilde{\theta} = -Y^2 \tilde{\theta}^3 \left(\frac{\tilde{\theta}}{Y} \right)' + \frac{1}{\epsilon} Y^2 \tilde{\theta}^3 , \tag{31}$$

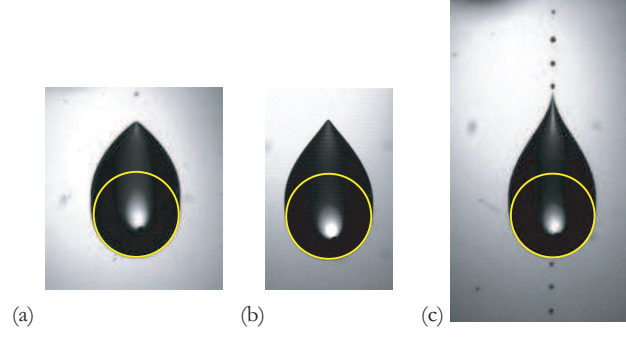which is a second-order equation for the drop profile $Y(\xi)$.

FIG. 5: Drops of viscosity 104 cP at different regimes: (a) corner, (b) cusp and (c) rivulet. The corresponding values of Ca/Ca_{riv} are 0.761, 0.975 and 1.047 respectively. In all cases the front of the drop is fitted extremely well by a circle.
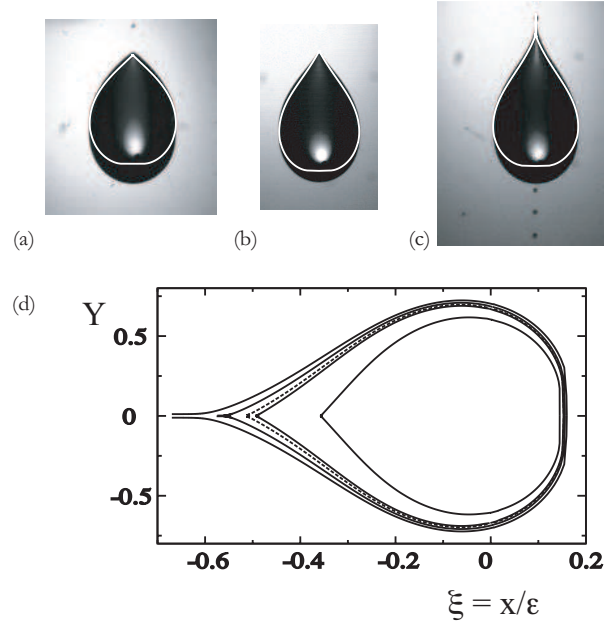

FIG. 6: (a-c) Same as in Fig. 5 compared to numerical simulation of Eq. (31). We fixed $\mathcal{C}/\mathcal{C}_{riv}$ at the corresponding experimental values Ca/Ca_{riv}. The only adjustable parameter here is the length scale of the numerical curves. The experimental profiles systematically have a larger aspect ratio due to contact angle hysteresis. (d) Dimensionless drop profiles obtained from Eq. (31) for various $\mathcal{C}$. The dashed curve corresponds to $\mathcal{C}_{riv}$.

All solutions of (31) end in a corner at the rear of the drop, with an opening angle Φ given by (29). One easily verifies that the asymptotic solution near the tip is of the form

$$Y' = \Phi + \beta Y^\alpha , \tag{32}$$

where $\alpha \simeq 6 - \frac{1}{\mathcal{C}\Phi} + \mathcal{O}(\epsilon^2)$ is fixed by $\mathcal{C}$ and ϵ, while β is a constant of integration. Thus using (32) as an initial condition, we integrate (31) numerically, adjusting β to match to the circular solution in front of the drop. As explained in more detail in Appendix A, this procedure selects a unique solution for a given value of the capillary number.

A sequence of profiles is shown in Fig. 6 for increasing capillary number. First, we reiterate that *all* solutions exhibit a corner, so our approximation is not able to capture the transition of a rounded drop toward a cornered state. This effect is clearly visible in Fig. 6a, and is due to our assumption of $\partial_{xx}h \ll \partial_{yy}h$, which breaks down at a rounded back. A related problem occurs at the very front of the drop, which at finite capillary number has a small flat portion (cf. Fig. 6). However, this artefact of our approximation does not affect the selection of the drop profile. As the capillary number is increased, the opening angle of the corner decreases according to (29). Interestingly, the drop shape is convex for moderate capillary number, but the profile develops a turning point at $\mathcal{C}_{cusp} \approx 0.66 \mathcal{C}_{riv}$. This feature agrees with experimental observation, as seen in Fig. 5, although experimentally the turning point is observed at values around $0.9 \mathcal{C}_{riv}$. This may be again be due to the regularization of the corner singularity, which is beyond the present description. In earlier publications, the appearance of a turning point was interpreted as the transition toward a cusp [6]. However, we stress that the present theory always predicts corners close to the tip. Let us also note that the experimental profiles display a vertical zone at the maximal width that is due to contact angle hysteresis. This is why the numerical profiles are systematically shorter than the experimental ones.

Finally, the dashed outline in Fig. 6d marks the critical capillary number $\mathcal{C}_{riv}$. Above $\mathcal{C}_{riv}$ no corner profiles are possible; namely, YY'' remains finite for $Y \to 0$, and hence Y'' diverges near the tip. Instead, rivulet solutions are found, which have a finite Y_r, as will be discussed in the next section.

C.   The drop speed

Up to now we have used the speed $\mathcal{C}$ as the control parameter. In the experiments [6] the drop volume is held fixed, while the inclination angle α is varied. It is found that the speed depends linearly on the *effective* Bond number

$$\text{Bo}_\alpha = V_{\exp}^{2/3}(\rho g/\gamma)\sin\alpha, \tag{33}$$

but the experimentally observed slope depends on viscosity. To compare to the theoretical prediction, we introduce the dimensionless volume

$$V_0 = \frac{1}{\theta_e}\int dx\, A(\xi) = \frac{2}{3\epsilon}\int d\xi\, \tilde{\theta}\, Y^2 \ , \tag{34}$$

so that V_0 depends on $\mathcal{C}$ and ϵ only.

The volume is well-defined for cornered drops; to extend (34) to rivulet solutions, we have to truncate the rivulet. Namely, we cut off the integration when $Y = 1.1 Y_r$. Close to the transition there is little volume inside the rivulet so that the volume is nearly independent of the precise cut-off value. We translate this into a real drop volume, $V_{\exp} = \theta_e V_0 L^3$, where L is the length scale (30). It is easily verified that (33) is related to V_0 by

$$\text{Bo}_\alpha = 4\theta_e^{5/3}\, V_0^{2/3} \ . \tag{35}$$

Figure 7 demonstrates that the numerically calculated Bo_α is indeed a nearly linear function of the capillary number, in agreement with experiment. Moreover, the experimental data collapse onto a single curve when considering $\text{Bo}_\alpha/(4\theta_e^{5/3})$ as a function of Ca/Ca_{riv}, confirming the rescaling of (35).

The main effect that has not been taken into account in our theoretical description is contact angle hysteresis, which is about 5-10° in the present experiments. As a result, drops only start to move once Bo_α is raised above a critical value [6, 35]. Instead, the numerical curve in Fig. 7 passes through the origin.

IV.   THE RIVULET

We now study the drop shape above $\mathcal{C}_{riv}$, where a rivulet appears. Experimentally, the rivulet breaks up into droplets, owing to an instability akin to the classical Rayleigh-Plateau
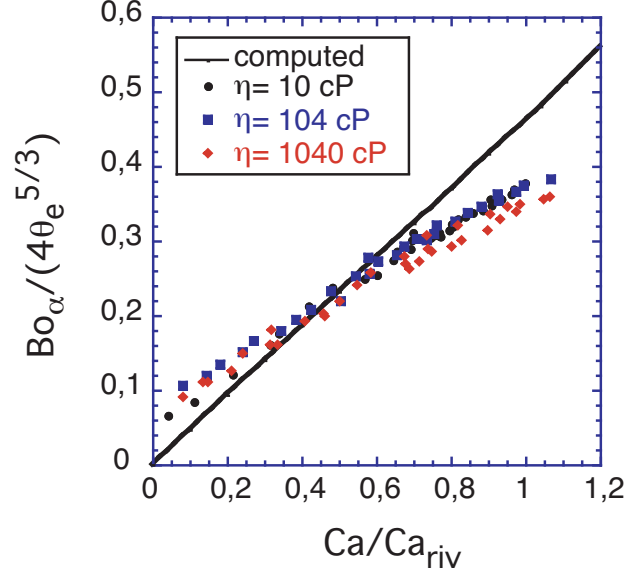
FIG. 7: The rescaled Bond number as function of $\mathcal{C}$. As predicted by (35), the experimental for different viscosities collapse onto a universal curve. To compute the theoretical curve, we chose a typical value of $\epsilon = 1/\sqrt{10}$. Theory somewhat overestimates the slope and does not display the off-set at $Ca = 0$ due to contact angle hysteresis.

instability [36]. We model the rivulet as a channel of constant width Y_r, which extends to infinity in one direction and is connected to a drop in the other direction. It is not possible to obtain the value of Y_r by considering the rear of the drop in isolation: (21) has no intrinsic length scale. Such a length is introduced by solving for the entire drop shape, as we have done in the previous section by including gravity into the description. Gravity introduces the modified capillary length (30) into the problem, which is related to the drop size via (35).

Instead of (31) we have to to reintroduce the constant of integration characterizing the flux through the rivulet:

$$\frac{35}{6}\mathcal{C}\left[\tilde{\theta} - \left(\frac{\tilde{Y}_r}{Y}\right)^2\right] = -Y^2\tilde{\theta}^3\left(\frac{\tilde{\theta}}{Y}\right)' + \frac{1}{\epsilon}Y^2\tilde{\theta}^3 . \tag{36}$$

The actual rivulet size is not identical to constant of integration $\tilde{Y}_r$, because gravity introduces a small correction,

$$Y_r^2 = \frac{35\mathcal{C}\epsilon}{12} - \sqrt{\left(\frac{35\mathcal{C}\epsilon}{12}\right)^2 - \frac{35\mathcal{C}\epsilon}{6}\tilde{Y}_r^2} . \tag{37}$$
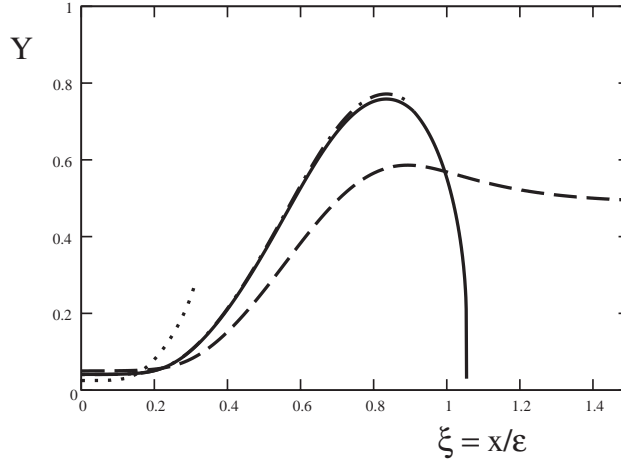
FIG. 8: Numerical solutions of (31) for $\mathcal{C} = 1.1\,\mathcal{C}_{riv}$ with different values for Y_r ($\epsilon = 0.316$). The drop solution (solid) is the separatrix between solutions that develop a singularity at finite height (dotted, dash-dotted) and those that reach a plateau (dashed). This provides a unique relation between Y_r and $\mathcal{C}$.

For a given value of the reduced capillary number $\mathcal{C}$, (36) selects a unique value of Y_r. We begin by describing how this value is found numerically. Namely, (36) is integrated with initial condition $Y = Y_r$, and a very small value of Y', cf. Fig. 8. The solution is constant at first (the rivulet) and then grows, giving four different types of solutions.

If the initial width is much too small, i.e., Y_r well below the correct value, the equation develops a singularity at which $\tilde{\theta} \to 0$ at a finite Y (dotted curve). If on the other hand the initial width is too large, the solution approaches a plateau (dashed) and extends to infinity. In the plateau region viscous forces and gravity are balanced. When decreasing the value of Y_r, the desired drop solutions are found as a *separatrix* (solid line) between solutions that reach the plateau and those who do not. The latter solutions which are close to the separatrix develop a singularity with a diverging second derivative Y'' at a finite value of $\tilde{\theta}$ (dash-dotted line). The origin of this singularity is explained in more detail in Appendix A below, where we show that the separatrix is indeed the only solution corresponding to a droplet with $Y = 0$ at the front. Thus there is indeed a unique drop solution of (31), which selects the value of Y_r.

In Fig. 9 the resulting Y_r, normalized by the maximum width of the drop Y_d, is plotted as function of $\mathcal{C}/\mathcal{C}_{riv}$ as the full line. Our theory predicts the existence of a universal curve, independent of the value of the inclination angle α. The rivulet size vanishes at $\mathcal{C}_{riv}$ and
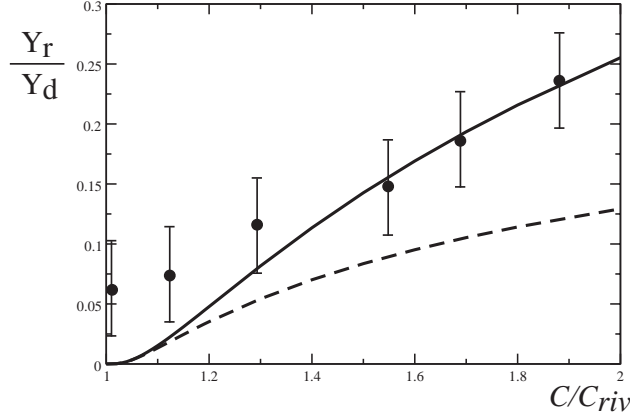
FIG. 9: The rivulet size Y_r (normalized by the maximum drop width Y_d) as a function of $\mathcal{C}$ as obtained from numerical resolution of (36) ($\epsilon = 0.344$, taken from experiment). Dots are experimental measurements. Close to the transition, the rivulet immediately starts to break up in a sinusoidal mode; in that case Y_r is taken as the average width. The dashed line corresponds to (38), with $\bar{Y} = 0.37$ and $a = 1.0515$.

increases with drop velocity. Close to the critical point the rivulet width is described by

$$Y_r = \bar{Y} \exp\left(-\frac{a}{\sqrt{\mathcal{C}/\mathcal{C}_{riv} - 1}}\right) , \tag{38}$$

with parameters $\bar{Y}$ and a that depend on ϵ. The dashed line shows that (38) well approximates our numerical results, in a region of capillary number within 10% of the transition value, with $a = 1.0515$. In App. B we perform an asymptotic analysis of (36) for small ϵ to show that (38) is indeed valid, with $a = \pi\sqrt{2}/6 \approx 0.740$, in the limit $\epsilon \to 0$.

Finally, the solid circles in Fig. 9 are experimental values. In computing $\mathcal{C}/\mathcal{C}_{riv} = Ca/Ca_{riv}$, we use the highest experimental value of Ca where corners are observed. As seen in Fig. 5, the rivulet soon breaks up into droplets, in particular close to the transition, where the rivulet width is small. Breakup is preceded by a wavy instability of the rivulet. When determining Y_r experimentally, we take the *average* of the minimum and the maximum width of a rivulet. The agreement between our theoretical prediction and experiment is quite satisfactory, again without any adjustable parameters, but experiment cannot confirm that the rivulet width goes to zero close to the transition. We suspect that this disagreement is due to our assumption of infinitely long, straight rivulets. In reality (cf. Fig. 5(c)), rivulets are quite short close to the transition, before they break up into droplets.

In particular, our calculation does not include the highly curved end of the rivulet, which pulls it back into the drop. One should also note that the experimental resolution (≈ 0.04 mm) becomes of the order of the rivulet width close to the transition.

V. CONCLUSIONS

We have analyzed drops sliding down an inclined plane within the lubrication approximation. Our asymptotic analysis for slender drops captures the transition from cornered drops to the deposition of a rivulet above a critical velocity. Within this framework we have obtained analytical and numerical results on the opening angle of the drop, the width of the rivulet, and the drop velocity, that compare well to experimental measurements. We obtain a second-order differential equation for the drop shape. Profiles obtained from numerical integration of this equation are very realistic as well. However, we do not explicitly treat the interface curvature along the direction of the drop speed. An important consequence of this is that the rear of the drop is always cornered, so that the transition towards a corner lies beyond the model. For a treatment of the regularization of the corner we refer to [21], for which the curvature along the drop motion is indeed shown to be dominant.

The main result of the paper is the speed-angle relationship (23), which entails the vanishing of the corner at a maximum velocity. This phenomenon remained unexplained in previous theories that assumed that the contact line's normal speed was kept at a constant value [5, 16, 22]. This assumption neglects the viscous flow between the two inclined contact lines and permits the corner angle ϕ to go to zero. Intuitively, the transition toward a rivulet may be understood by the following mechanism: the interface curvatures are much greater near the corner tip than away from it, providing a pressure gradient to drive the viscous flow toward the drop. In the limit where the corner angle goes to zero, however, the corner becomes more and more like a rivulet with parallel contact lines, for which these pressure gradients disappear. Hence the balance between surface tension driving and viscous resistance can no longer been maintained. Our arguments show the transition toward a rivulet to be governed by the three-dimensional structure of the contact line, as opposed to the transition of a single straight contact line [12, 15]. In particular, this results in the critical capillary number to have the anomalous scaling $Ca_{riv} \propto 1/\overline{\ln}^{1/2}$ (cf. Eq. (19)), instead of the usual dependence on $1/\overline{\ln}$ [15].

The comparison to experimental data in Fig. 3 shows that the proposed rescaling of capillary number and angle results in a collapse of data for liquids of widely varying viscosities. Yet, there are some quantitative disagreements with the theoretically predicted speeds. We believe this to be due to the our approximation of the cross-section of the drop by a parabola, which is valid only for $\epsilon \to 0$. In a more general description using the similarity solutions introduced in [20], one would have to match to the logarithmically varying Cox-Voinov solution Eq. (17) near the contact line. Technically, this turns out to be a difficult task, since the parameters of the Cox-Voinov solution must vary along the contact line. Thus a match can perhaps only be achieved by introducing yet another intermediate region. Instead, we have used a simple 'patching' procedure by equating the two solutions at a single point of an intermediate length scale $\overline{x}$, which induces a small error of logarithmic order.

Finally, the results for the corner structure are independent of the global drop geometry: the outer geometry only induces a small correction that vanishes at the corner tip, cf. Eq. (32). This suggests that cornered contact lines observed e.g. when a plate is withdrawn from a liquid reservoir should follow the same universal relation between ϕ and Ca. In the case of a rivulet, a characteristic length scale was set by the size of the drop. It still needs to be investigated which parameter sets this length scale in other geometries.

APPENDIX A: ORIGIN OF THE SEPARATRIX

The selection mechanism for the drop shown in Fig. 8 as the full line is best understood by considering the function $\tilde{\theta}(Y')$ given in (27). It possesses a maximum at some negative value of Y' (cf. Fig. 10), i.e. at the front of the drop. Let us follow a solution starting at the rivulet, $(Y' = 0, \tilde{\theta} = 1)$, which evolves toward positive Y'. Without the effect of gravity, this solution continues until it reaches $\tilde{\theta} = 0$, beyond which the boundary condition becomes unphysical. This happens for small values of Y_r.

For larger values of Y_r, the effect of gravity will eventually stop the increase of Y' so that the point $\tilde{\theta} = 0$ is avoided. Solutions then return along the right branch of Fig. 10. Now, there are two possibilities: the solutions either relax towards $Y' = 0$, $\tilde{\theta} = 1$, or attain the maximum possible value of $\tilde{\theta}$. The first case corresponds to the 'plateau' solutions of Fig. 8,
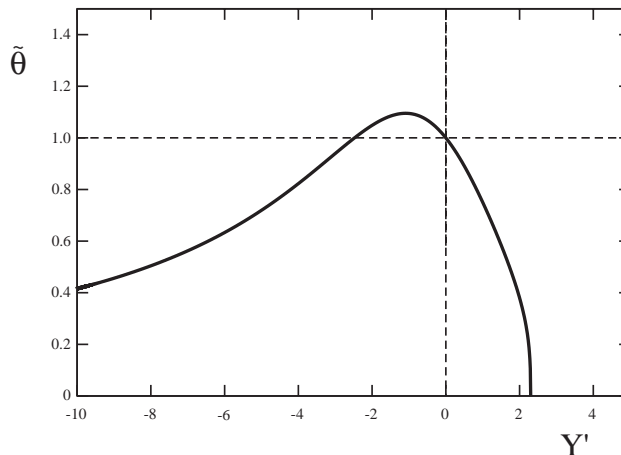
FIG. 10: The function $\tilde{\theta}(Y')$ according to (27), plotted with $\epsilon = 1/\sqrt{10}$ and $\mathcal{C} = 3/2\mathcal{C}_{cr}$. The maximum of this curve plays a crucial role in the selection of the drop solution (see text).

(dashed), which indeed have $Y' = 0$. The other solutions run into a singularity at finite height Y (dash-dot). Namely, the derivative $\tilde{\theta}'$ can be written as

$$\tilde{\theta}' = Y'' \frac{d\tilde{\theta}}{dY'} \; . \tag{A1}$$

When the maximum value of $\tilde{\theta}$ is reached, one obviously has $d\tilde{\theta}/dY' = 0$, so that Y'' has to diverge to compensate the other terms in (31). The only exception is when the other terms vanish, so that $\tilde{\theta}' = 0$ and a finite Y'' is allowed. Only in this particular case, the solutions will continue along the left branch of Fig. 10, eventually leading to $Y' \to -\infty$. This is precisely the separatrix between the two behaviors.

So the governing equation (31) indeed has the property that only one solution can connect a rivulet to a drop front that has $Y = 0$. The reason is that one requires the unique condition of $\tilde{\theta}' = 0$ as $\tilde{\theta}$ reaches its maximum, to make it possible to pass the maximum and continue on towards $Y' \to -\infty$. Let us note that the incorporation of the $\sqrt{1 + (\epsilon Y')^2}$ denominators in (27) are crucial for the drop solution: without these terms $\tilde{\theta}$ no longer exhibits a maximum and solutions always return to $Y' = 0$.

APPENDIX B: THE SCALING OF Y_r IN THE LIMIT $\epsilon \to 0$

We mentioned that (21), which does not incorporate the effect of gravity, has no intrinsic length scale and thus cannot determine the rivulet size Y_r. However, this equation has an

analytical solution, which remains valid as long as $Y_r \ll Y \ll Y_d$, where Y_d is the maximum drop width. The result is thus an intermediate solution, which connects between the rivulet and the front of the drop. Close to $\mathcal{C}_{riv}$, Y_r/Y_d goes to zero; we use this scale separation to find simplified matching conditions for the intermediate solution to connect to the rivulet on one side, and a rounded drop on the other.

Namely, for $Y_r = 0$ (21) and (22) simplify to

$$\frac{35}{6} = YY'' + (1/\mathcal{C} - 3Y')\,Y' \ , \tag{B1}$$

which can be solved by putting $Y' = F(Y)$:

$$\frac{35}{6} = YF\frac{dF}{dY} + (1/\mathcal{C} - 3F)\,F \ . \tag{B2}$$

Separating variables, we find that

$$\ln\frac{Y}{Y_0} = \frac{1}{6}\ln\left(35\mathcal{C} - 6F + 18\mathcal{C}F^2\right) + \frac{1}{3D}\arctan\left(\frac{6\mathcal{C}F - 1}{D}\right) \ , \tag{B3}$$

where $D = \sqrt{70\mathcal{C} - 1}$. Writing $\mathcal{C} = \mathcal{C}_{riv} + \delta$, one finds $D \simeq \sqrt{140\mathcal{C}_{riv}\delta}$, so we are interested in the limit $D \ll 1$.

Solutions (B3) start with vanishing slope $Y' = F = 0$ at the rivulet, with F increasing monotonically toward the front of the drop. Without gravity, F continues to increase, until a singularity $F = 1/(3\mathcal{C})$ is reached, which corresponds to the dotted line in Fig. 8.

Thus the matching condition at $Y_d = Y \gg Y_r$ is that the argument of the arctan is positive, which in the limit $\delta \to 0$ gives

$$\ln(Y_d/Y_0) \simeq \frac{\pi}{6\sqrt{140\mathcal{C}_{riv}\delta}} \ . \tag{B4}$$

For $F = 0$, on the other hand, the sign of the arctan is negative, and we have

$$\ln(Y_r/Y_0) \simeq -\frac{\pi}{6\sqrt{140\mathcal{C}_{riv}\delta}} \ . \tag{B5}$$

Combining the two, we indeed obtain (38) with $a = \pi\sqrt{2}/6 \approx 0.740$. To also obtain an expression for $\bar{Y}$, a much more detailed analysis would be necessary, which performs the matching to the rounded part of the drop explicitely.

As seen in Fig. 11, the theoretical scaling result (38) fits the numerics quite well: while for $\epsilon = 0.344$ we find $a = 1.0515$, we obtain $a = 0.825$ for $\epsilon = 0.15$, which is approaching
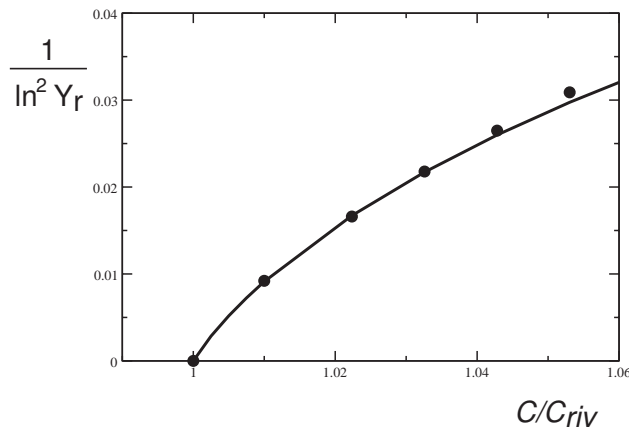
FIG. 11: Numerical test of the analytical formula (38) for the drop width for $\epsilon = 0.15$. The full line is a fit, $a = 0.825$ and $\bar{Y} = 2.21$, of numerical data (circles).

the asymptotic value of $a = 0.740$. The prefactor $\bar{Y}$, which we were not able to calculate, is empirically found to be of the order of the drop width.

[1] C. Huh and L. E. Scriven, " Hydrodynamic model of steady movement of a solid/liquid/fluid contact line", J. Coll. Int. Sci. **35**, 85 (1971).

[2] P. A. Thompson and M. O. Robbins, " Simulations of contact-line motion: slip and the dynamic contact angle", Phys. Rev. Lett. **63**, 766 (1989).

[3] P. G. de Gennes, " Wetting: statics and dynamics", Rev. Mod. Phys. **57**, 827 (1985).

[4] L. M. Hocking, " Rival contact-angle models and the spreading of drops", J. Fluid Mech. **239**, 671 (1992).

[5] T. Podgorski, J. M. Flesselles, and L. Limat, " Corners, cusps, and pearls in running drops", Phys. Rev. Lett. **87**, 036102(1) (2001).

[6] N. Le Grand, A. Daerr, and L. Limat, " Shape and motion of drops sliding down an inclined plane", J. Fluid Mech. **541**, 293 (2005).

[7] R. V. Roy, Stability and nonlinear evolution of capillary ridges and rivulets, Euromech Fluid Mechanics Conference, Toulouse, book of abstracts, 2003.

[8] L. W. Schwartz, D. Roux, and J. J. Cooper-White, "On the shapes of droplets that are sliding on a vertical wall", Physica D **209**, 236 (2005).

[9] P. G. Simpkins and V. J. Kuck, " On air entrainment in coatings", J. Col. Interf. Sci. **263**,

562 (2003).

[10] D. Quéré, " On the minimal velocity of forced spreading in partial wetting (in French)", C. R. Acad. Sci. Paris, Serie II **313**, 313 (1991).

[11] R. V. Sedev and J. G. Petrov, " The critical condition for transition from steady wetting to film entrainment", Colloids and Surfaces **53**, 147 (1991).

[12] J. H. Snoeijer, G. Delon, M. Fermigier, and B. Andreotti, "Avoided critical behavior in dynamically forced wetting", Phys. Rev. Lett. **96**, 174504 (2006).

[13] L. D. Landau and B. V. Levich, " Dragging of a liquid by a moving plate", Acta physico-chimica USSR **17**, 42 (1942).

[14] B. V. Derjaguin, " On the thickness of a layer of liquid remaining on the walls of vessels after their emptying, and the theory of the application of photoemulsion after coating on the cine film", Acta physico-chimica USSR **20**, 349 (1943).

[15] J. Eggers, " Existence of receding and advancing contact lines", Phys. Fluids **17**, 082106 (2005).

[16] T. D. Blake and K. J. Ruschak, " A maximum speed of wetting.", Nature **282**, 489 (1979).

[17] S. Kistler, Hydrodynamics of wetting, in *Wettability*, edited by J. C. Berg, Marcel Dekker, New York, 1993.

[18] J. G. Petrov and R. V. Sedev, " On the existence of a maximum speed of wetting", Colloids Surfaces **13**, 313 (1985).

[19] H. A. Stone, L. Limat, S. K. Wilson, J. M. Flesselles, and T. Podgorski, " Corner singularity of a contact line moving on a solid substrate", C. R. Physique **3**, 103 (2002).

[20] L. Limat and H. A. Stone, " Three-dimensional lubrication model of a contact line corner singularity", Europhys. Lett. **65**, 365 (2003).

[21] J. H. Snoeijer, E. Rio, N. Le Grand, and L. Limat, " Self-similar flow and contact line geometry at the rear of cornered drops", Phys. Fluids **17**, 072101 (2005).

[22] M. Ben Amar, L. Cummings, and Y.Pomeau, "Transition of a moving contact line from smooth to angular", Phys. Fluids **15**, 2949 (2003).

[23] E. Rio, A. Daerr, B. Andreotti, and L. Limat, " Boundary Conditions in the Vicinity of a Dynamic Contact Line: Experimental Investigation of Viscous Drops Sliding Down an Inclined Plane ", Phys. Rev. Lett **94**, 024503 (2005).

[24] A. Oron, S. H. Davis, and S. G. Bankoff, " Long-scale evolution of thin liquid films", Rev.

Mod. Phys. **69**, 931 (1997).

[25] C. L. Navier, " Sur les lois du mouvement des fluides", Mem. Acad. R. Sci. France **6**, 389 (1827).

[26] E. Lauga, M. P. Brenner, and H. A. Stone, *The no-slip boundary condition: a review*, page ???, 2005.

[27] C. Cottin-Bizonne, B. Cross, A. Steinberger, and E. Charlaix, " Boundary slip on smooth hydrophobic surfaces: intrinsic effets and possible artifacts", Phys. Rev. Lett. **94**, 056102 (2005).

[28] M. Eres, L. Schwartz, and R. Roy, " Fingering phenomena for driven coating films", Phys. Fluids **12**, 1278 (2000).

[29] J. Eggers, " Toward a description of contact line motion at higher capillary numbers", Phys. Fluids **16**, 3491 (2004).

[30] J. M. Davis, " Asymptotic analysis of liquid films dip-coated onto chemically micropatterned surfaces", Phys. Fluids **17**, 038101 (2005).

[31] O. V. Voinov, " Hydrodynamics of wetting [English translation]", Fluid Dynamics **11**, 714 (1976).

[32] R. G. Cox, " The dynamics of the spreading of liquids on a solid surface. Part 1. Viscous flow", J. Fluid Mech. **168**, 169 (1986).

[33] L. M. Hocking, " The spreading of a thin drop by gravity and capillarity", Q. J. Appl. Math. **36**, 55 (1983).

[34] L. Limat et al., "Shape of drops sliding down an inclined surface", Proceedings of 4th European Coating Symposium, Bruxelles, 1-4 october 2001 (2002).

[35] E. B. Dussan V. and R. T.-P. Chow, " On the ability of drops or bubbles to stick to non-horizintal surfaces of solids", J. Fluid Mech. **137**, 1 (1979).

[36] P. C. Duineveld, "The stability of ink-jet printed lines of liquid with zero receding contact angle on a homogeneous substrate", J. Fluid Mech. **477**, 175 (2003).